GEORG-AUGUST-UNIVERSITÄT GÖTTINGEN

Fakultät für Physik

Bachelor's Thesis

Sensitivitätsstudien von Operatoren der effektiven Feldtheorie in trileptonischen tZq-Endzuständen

Sensitivity studies of effective field theory operators in trileptonic tZq final states

prepared by

Tim Schlömer

from Cloppenburg

at the II. Physikalischen Institut

Thesis number:	II.Physik-UniGö-BSc-2022/07
Thesis period:	18th April 2022 until 25th July 2022
First referee:	Prof. Dr. Arnulf Quadt
Second referee:	Prof. Dr. Stan Lai

Zusammenfassung

In dieser Arbeit wird der Einfluss von Operatoren der effektiven Feldtheorie in der Produktion von einzelnen Top-Quarks in Assoziation mit einem Z-Boson und einem weiteren Quark am ATLAS Detektor am LHC untersucht. Effektive Feldtheorie ist ein Ansatz für Theorien jenseits des Standardmodells, um die Schwächen des Standardmodells zu erklären.
Ziel dieser Arbeit ist die Bestimmung von Ausschlussgrenzen für die Stärke der Operatoren. Dazu werden zunächst sensitive Observablen bestimmt, um den Einfluss der Operatoren zu quantifizieren und anschließend den mögliche Einfluss abzugrenzen.

Stichwörter: Teilchenphysik, top Quark, BSM, EFT

Abstract

In this thesis, the influence of effective field theory operators in the production of single top quarks in association with a Z boson and another quark is investigated at the ATLAS detector at LHC. Effective field theory is an approach for theories beyond the Standard Model to explain the weaknesses of the Standard Model.
The aim of this work is to determine exclusion limits for the strength of the operators. For this purpose, sensitive observables are first determined in order to quantify the influence of the operators and then used to limit the possible influence.

Keywords: Particle physics, top quark, BSM, EFT

Contents

1. Introduction

The question of what the world is made out of is probably one of the oldest scientific questions. With technological progress, this question could be answered on smaller length scales and with higher precision. Today, physics on smallest length scales is called "particle physics" and can still not fully answer the question, therefore work is not yet complete. The current understanding of particle physics is summed up in the standard model in a precise way. But it is already known to be incomplete, and further research is needed.
In this thesis, I will be looking at an approach of physics beyond the Standard Model called Effective Field Theory (EFT). For the analysis, the impacts of EFT operators in multiple observables are studied, with the goal of setting a limit on the strength of these influences.
To begin with, a short theoretical overview of the Standard Model, top quark physics and EFT is given in Chapter 2. Then the experimental setup of the Large Hadron Collider Lhc with the Atlas detector is described in Chapter 3. Afterwards, in Chapter 4 the object definitions are given, while Chapter 5 shows the event selection for the analysis. In chapter 6 the sensitivity study is explained, with the results being shown in Chapter 7. A conclusion with an outlook is given in Chapter 8.

2. The Standard Model of Particle Physics

The Standard Model (SM) describes the elementary particles and their interaction via the strong, the weak and the electromagnetic force. Not included is the gravitational force, therefore it is already known the SM is incomplete. Apart from that, the SM is able to predict the nature and behaviour of the elementary particles with remarkable precision across a vast range of scales.

2.1. Elementary particles and their interaction

The SM consists of gauge-invariant quantum field theories (QFTs) with the symmetry group SU(3) $\times$ SU(2) $\times$ U(1). The symmetry group SU(3) describes the strong interaction via quantum chromodynamics (QCD), SU(2) describes the weak interaction (quantum flavourdynamics, QFD) and U(1) is used for the electromagnetic interaction (quantum electrodynamics, QED) [1, 2].
The SM differentiates between fermions with spin $\frac{1}{2}$ and bosons with integer spin. Fermions are further divided into quarks and leptons as well as corresponding antifermions with the same mass, but opposite electric charge. The elementary particles can be seen in Figure 2.1, where quarks are shown on the upper left, leptons on the lower left, and bosons on the right. Fermions are divided in three generations, i.e. up and down quark with electron and electron neutrino forming the first generation. Charm and strange quark form the second generation with the muon and its neutrino. Finally, with top and bottom quark as well as tau and tau neutrino being the third generation, there are twelve fermions. All fermions with negative helicity (called left-handed) are described by a weak isospin doublet and are therefore sorted in pairs. They are divided by the third component of their weak isospin (I_3) into up- and down-type fermions. The up-type quarks with $I_3 = 1/2$ include the up, the charm and the top quark. Meanwhile the down, the strange and the bottom quark are the down-type ($I_3 = -1/2$) quarks. For the leptons, the neutrinos are the up-type fermions, and the charged leptons (electron, muon, tau) are down-type. The

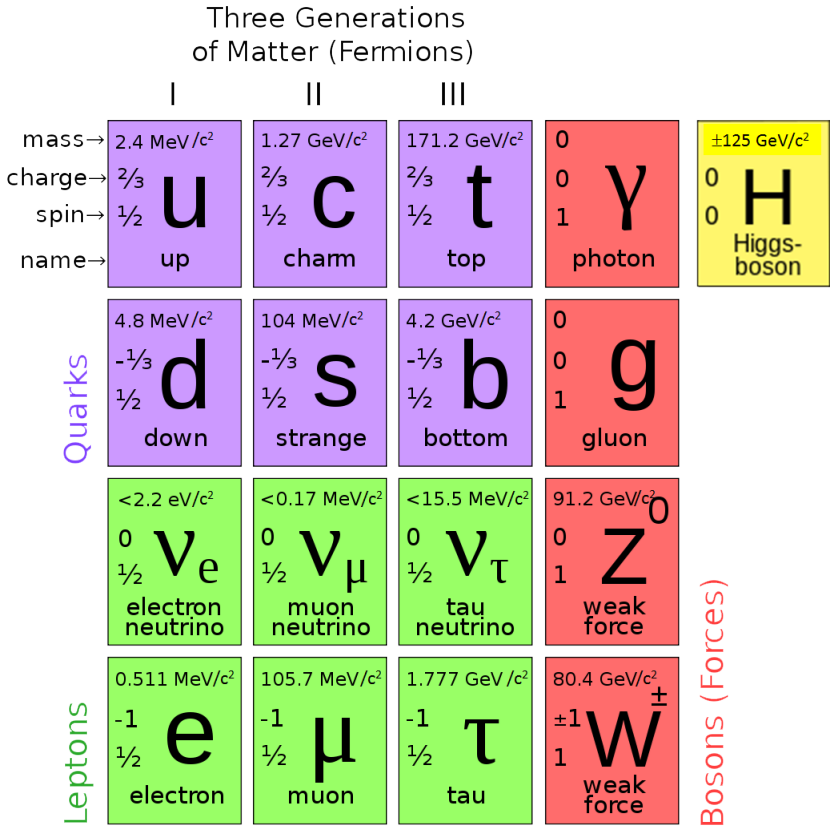

Figure 2.1.: Particle content of the SM of particle physics.

doublets allow weak transitions between the different particles. The right-handed (positive helicity) fermions form singlets, which do not allow weak transitions between them. Quarks have either an electric charge of $\frac{2}{3}$ or $-\frac{1}{3}$. Leptons have an electric charge of 0 for the neutrinos and -1 for electron, muon and tau. According to the strong interaction, every (anti-)quark carries one of the three (anti-)colour charges, while gluons carry a charge of a colour and an anticolour combined. The other elementary particles are colourless. Since bound states always have to be colourless, quarks bind with other quarks to form hadrons. This is called hadronisation and is a basic concept of QCD. If a coloured state is produced in an experiment, it will produce other quarks around them to create a colourless state. The timescale $\tau_{had} \sim 10^{-23}$[3] of this process is small, therefore bare quarks are not directly observable. If these bound states decay, even more quarks are created, therefore more quarks are registered in close distance to each other. In the experimental description, multiple hadrons originating from a high-energy quark in a collimated stream are called jets.

The bosons are the force mediators in the SM. The photon and the gluon have spin 1, are massless, have no electric charge, and serve as the mediators of the electromagnetic force

and the strong force, respectively. The W and Z bosons mediate the weak interaction. The W boson has either electric charge $+1$ or -1, a mass of 80 GeV [4] and spin 1. The Z boson also has spin 1, while its electromagnetic charge is 0 with a mass of 91 GeV [5]. The last boson to be introduced is the Higgs boson, which is the boson of the Brout-Englert-Higgs mechanism [6] in the SM. The coupling of the fermion fields to the Higgs field via the Higgs boson is responsible for the mass of the fermions. The Higgs boson has spin and electric charge 0 with a mass of 125 GeV [7]. The mechanism was introduced to explain the masses of the W and Z boson, which would otherwise be massless in the SM. Due to the spontaneous symmetry breaking of the electro-weak interaction, W and Z boson acquire their masses. For fermions, this introduces the Yukawa-coupling between the fermion field and the Higgs field which leads to gauge-invariant masses for the fermions.

2.2. The top quark

The top quark is studied extensively because of its high mass of $172.08 \pm 0.39\,(\text{stat.}) \pm 0.82\,(\text{syst.})$ GeV [8], which indicates a strong Yukawa-coupling. The top quark was discovered in 1995 by DØ and CDF at the Tevatron [9, 10]. Its measured properties are consistent with a predicted electric charge of $\frac{2}{3}$ and spin $\frac{1}{2}$. The top quark is predicted to be an up-type quark, but so far there are no direct measurements of I_3.
The top quark has a lifetime of $10^{-25}\,\text{s}$ [3]. Therefore, it decays before it hadronises, and also before spin decorrelation ($10^{-21}\,\text{s}$). Consequently, the spin information of the top quark is passed on to its decay products. The Cabibbo Kobayashi Maskawa (CKM) matrix shows that the top quark will almost always decay into a bottom quark via emission of a W boson. This W boson can then decay either into a quark-antiquark pair or a charged lepton and its neutrino.
For this thesis, the production of a single top quark associated with a Z boson is studied. The relevant Feynman diagrams are shown in Figure 2.2. The relevant force for all of these processes is the weak interaction, since it is the only force to allow a flavour change. The two main processes are W boson exchange with Z emission from any of the involved quarks. Another possible process is the W fusion into a Z boson [11]. The SM vertex for a Z production process is equal to $i(v_f - a_f\gamma^5)\sqrt{\alpha}\gamma^\mu$ where v_f and a_f are vector and axialvector coupling parameters of the weak force, which depend on the fermion, α is the weak coupling strength and γ are the Dirac-matrices.
This process is observed via the decay of $tZq \to Wb\ell^-\ell^+q$, where ℓ is a charged lepton, and only the Z decay to two leptons is considered. Furthermore, the W boson decay into 2 leptons is required. The trileptonic final state is chosen to reduce the background con-

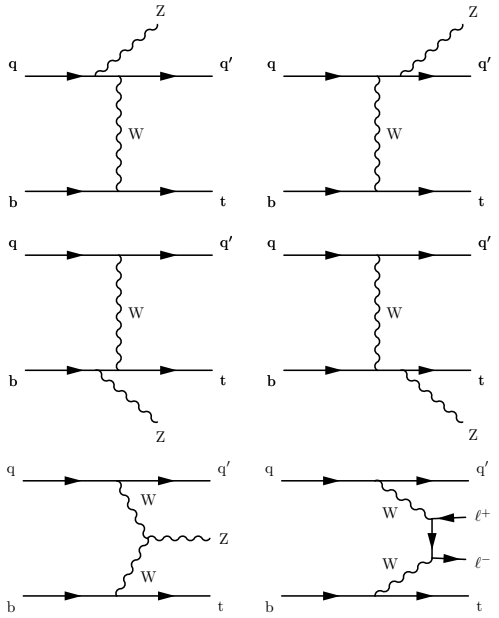

Figure 2.2.: Feynman graphs for tZq production, with a non-resonant process on the bottom right.

tributions, as hadronic processes have larger backgrounds than leptonic ones. Also, the focus on leptonic decays is based on the better sensitivity in polarisation measurements. The polarisation of the top quark describes the alignment of its spin to a given direction. Since quarks form hadrons, the polarisation properties of the W/Z and top quark are lost, while leptons keep the polarisation and spin of the W/Z boson. Since the top quarks are produced via the weak interaction, they can be polarised. This process is quite rare at the LHC with a SM cross section of 94 fb for leptons with an invariant mass greater than 30 GeV [11].

2.3. Beyond the Standard Model and effective field theory

Since the SM has several shortcomings, e.g. it can not explain the observed neutrino oscillation [12], the existence of dark matter and dark energy [13] nor the observed CP asymmetry [14]. Therefore, an abundance of theories beyond the SM exist, which attempt to explain these shortcomings. In this thesis, the relevant theory is the approach via an effective field theory (EFT) [15]. The basic assumption is that the SM can be interpreted as a low energy approximation of a more fundamental theory. Many theories beyond the SM include new particles or mechanisms which are not yet accessible with the current

particle accelerators. Instead, they influence processes in higher order, for example via loops in propagators. An example for this would be Fermi's theory of the β-decay as a four-fermion vertex, which is a low energy approximation of the exchange of a W boson in the SM. An SMEFT study can be used to search for influences of non-SM particles and identify differences between the SM-prediction and the measured data.
In this thesis, the influences of EFT operators in the tZq-process are studied. The suppression due to the energy scale is parameterised as $1/\Lambda^{d-4}$ and to preserve lepton and baryon number, the dimension has to be six [16]. The Lagrangian can then be written as

$$\mathcal{L} = \mathcal{L}_{SM} + \sum_i \frac{c_i}{\Lambda^2} \mathcal{O}_i \tag{2.1}$$

with the standard model Lagrangian $\mathcal{L}_{SM}$, the Wilson coefficients (WC) c_i, the energy scale Λ and the operators $\mathcal{O}_i$. The studied operators are $\mathcal{O}_{tW}$ (only real part) and $\mathcal{O}_{tB}$ (real and imaginary part) [17]. These operators in leading order can be written as

$$\mathcal{O}_{tW} = i(\bar{Q}\,\sigma^{\mu\nu}\,\tau_I\,t)\,\tilde{\varphi}\,W^I_{\mu\nu}$$
$$\mathcal{O}_{tB} = i(\bar{Q}\,\sigma^{\mu\nu}\,t)\,\tilde{\varphi}\,B_{\mu\nu}.$$

with τ_I being the Pauli matrices and W and B the Goldstone bosons of the electroweak theory. Since the weak bosons are linear combinations of the Goldstone bosons, the operators affect the coupling between top quark and the W/Z boson. The $\mathcal{O}_{tW}$ operator therefore influences the W and Z boson, which is relevant for the bWt and tZ couplings, while $\mathcal{O}_{tB}$ only influences the Z boson and therefore the tZ coupling.
The goal of this study is to extract exclusion limits on the WCs and therefore a limit on the influence of non-SM processes.

3. Experimental Setup

The experimental setup for the thesis is the ATLAS detector [18] at the Large Hadron Collider (LHC) [19] at CERN.

3.1. The Large Hadron Collider

The Large Hadron Collider is a circular hadron accelerator and collider with two beam pipes with four collision points. For the LHC, the relevant pre-accelerators are: Linac4 where the proton beams are produced via acceleration of H^--Ions, which lose their electrons on transition to the Proton Synchrotron Booster (PSB) where they are accelerated to 2 GeV and then transferred to the Proton Synchrotron (26 GeV) and the Super Proton Synchrotron (450 GeV) until they finally reach the LHC where the energy rises to 6.5 TeV. The LHC has a circumference of 27 km with about 10,000 superconducting magnets along the beam line with a magnetic field strength up to 7.7 T. At maximum energy, the protons reach more than 99.999 % of the speed of light. The proton beams are not continuous, but consist of bunches which are 25 ns apart from each other [19].
The two beams then collide in one of the four detectors ALICE [20], which studies heavy ion collisions to recreate the state of the universe shortly after the Big Bang, CMS [21], which studies the SM and theories beyond it, LHCb [22], which focuses on b quark physics, or the ATLAS detector, also focusing on the SM and theories beyond, which will be explained in detail in the next chapter.

3.2. The ATLAS detector

At ATLAS, an instantaneous luminosity in the order of 10^{34} $\mathrm{cm}^{-2}\mathrm{s}^{-1}$ can be achieved [18]. The ATLAS detector [18] can be seen in Figure 3.1. It has a cylindrical form with a diameter of 25 m and a length of 44 m. Therefore, cylindrical coordinates are used, with the z-Axis along the beam line, the azimuthal angle φ and the polar angle θ. Instead of the polar angle, the pseudorapidity $\eta = -\ln\left(\tan\frac{\theta}{2}\right)$ is used, neglecting the mass of the particle because of the high energy achieved in the collisions. It is able to

record many different particle properties. For this purpose, it has multiple elements. The Inner Detector (ID) consists of a pixel detector, a strip tracker and a transition radiation tracker and is embeded in a solenoid magnet with a field of 2 T. Around the ID, the electromagnetic and hadronic calorimeters are installed. The outermost layer is the muon spectrometer.

The ID measures the position of a particle in multiple layers. Because all particles with an electric charge have bent trajectories, it is possible to reconstruct the charge (from the direction of the curvature) and momentum of the particles. This is done by using the equality of the Lorentz force and central force, which gives $p = QBr$ with the electric charge Q, magnetic field strength B and curvature radius r. This is especially important for b quark jets, which can be identified because their relatively long life time leads to their jets originating from a secondary vertex instead of the primary collision.

In the calorimeters most particles deposit their energy, with the exception of muons, as they are minimally interacting particles (MIPs), and neutrinos, which do not interact with the detector at all.

In ATLAS both electromagnetic and hadronic calorimeters are used. The energy of the particles is reconstructed via measurement of the resulting electromagnetic or hadronic showers. The electromagnetic calorimeter uses liquid argon as detector medium and is used for the absorption of particles like electrons and photons, while the hadronic calorimeter has steel absorbing layers and scintillating tiles as active material, and is able to measure the energy of hadrons such as protons and neutrons. Protons and other charged hadrons will leave a trace in the electromagnetic calorimeter and then cause hadronic showers in the hadronic calorimeter. The jets reconstructed from the energy deposits in the calorimeters are important to reconstruct the particles produced at the primary collision [18].

The muon spectrometer tracks the trajectory of the muons similar to the ID. As already mentioned muons are MIPs, while they leave a trace in the ID and deposit energy in the calorimeters, they still reach the muon chambers. This is in contrast to the other particles, except neutrinos. Therefore, muons can be easily identified, since neutrinos do not interact with the muon chambers. Since the muon spectrometer is placed on the outside of the rest of the detector, it is actually the largest detector.

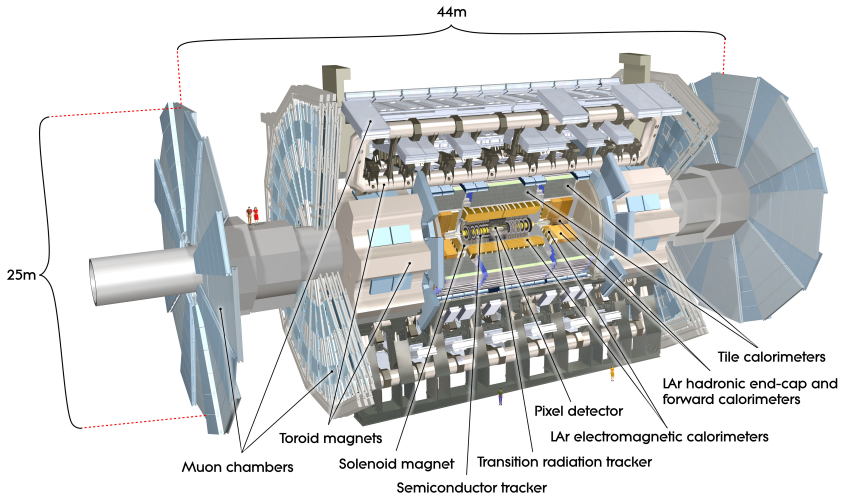

Figure 3.1.: Computer simulated image of the ATLAS detector. ©CERN

4. Object definitions and reconstruction

Electrons are reconstructed from energy clusters in the electromagnetic calorimeters which match with a reconstructed track [23]. They are required to have $|\eta| < 2.47$, but without the $1.37 < |\eta| < 1.52$ region, since this is the transition between barrel and calorimeters. The transverse energy E_T has to be at least 15 GeV. Additionally, the transverse impact parameter d_0 is defined, which is divided by its uncertainty $|d_0|/\sigma(d_0) < 5$. The longitudinal impact parameter z_0 is required to be $|z_0 \sin(\theta)| < 0.5$ mm [23].
Muons are reconstructed by the combination of a track in the muon chambers and a track in the ID. They are required to have $p_{\mathrm{T}} > 15$ GeV and $|\eta| < 2.5$. The impact parameter requirements are applied as well , with $|d_0|/\sigma(d_0) < 3$ and $|z_0 \sin(\theta)| < 0.5$ mm [24].
Jets are reconstructed with the anti-k_t algorithm [25] with $R = 0.4$ as radius parameter. The b-tagging is done via the "DL1r" algorithm [26], which uses the reconstructed track and secondary as well as tertiary vertex information. The working point (WP) is at 70%, therefore the jet has to have a b-tagging discriminant value larger than for a 70 % efficient selection.

5. Event selection

The event selection is important to maximise the number of signal event while minimising the number of unwanted background events. Therefore, several requirements are made to select suitable events for the analysis.

5.1. Trileptonic final state

After its production, the tZq-state decays into different final states. In this thesis, the studied decay mode consists of three leptons, and therefore is called trileptonic. The top quark decays into a b quark and a W boson, which then decays into a charged lepton and a neutrino. The Z boson decays into two charged leptons of the same flavour, but with opposite charge. The additional quark forms a light jet, so in total there are two jets, three charged leptons and a neutrino. Since neutrinos cannot be detected in the ATLAS detector, the missing transverse energy is reconstructed and associated with the neutrino, which is possible because there is only one neutrino in the final state [27].
The reconstruction of top and Z is useful to differentiate between signal and background processes. For example, if it is not possible to reconstruct a Z boson because there was no opposite sign same flavour (OSSF) lepton pair, the desired final state was not reached. The Z is easily reconstructed in $ee\mu$ and $e\mu\mu$ events as the addition of the respective lepton pair four-vectors. In final states with three leptons of the same flavour, the pair with the invariant mass closest to the Z is chosen.
In contrast, the reconstruction of the W boson is more complicated due to the neutrino produced in the leptonic decay. The lepton not used in Z reconstruction and the missing transverse energy are added, but the longitudinal part of the four-vector along the z-axis is still missing. It can be calculated via the mass of the W

$$M_W^2 = (P^W)^2 = (P^\ell + P^{\text{miss}})^2$$

with the solution

$$E_Z^{\text{miss}} = \frac{\alpha \cdot P_Z^\ell \pm \sqrt{(E^\ell)^2(\alpha^2 - p_t^\ell \cdot E_{\text{T}}^{\text{miss}})}}{(p_t^\ell)^2} \tag{5.1}$$

with

$$\alpha = \frac{1}{2} \cdot M_W^2 + \vec{p}_{\mathrm{T}}^{\,\ell} \cdot \vec{E}_{\mathrm{T}}^{\mathrm{miss}}.$$

If there are two real solutions E_Z^{miss}, the smaller result is used. If there are imaginary solutions, the missing transverse energy is considered incorrectly measured. By fixing the transverse mass of the W to the actual mass, and introducing another scale factor, one can recalculate E_T^{miss} [27].
The W boson and the b-tagged jet are then used to reconstruct the top quark.

5.2. Signal Regions

For this analysis, two signal regions are defined. In the first signal region (SR1), events with the exact expected final state of three leptons, one b tagged and one additional untagged jet are selected. In the second region (SR2), an additional radiation jet is required. The other requirements are identical for both regions.
For all of the jets, $p_{\mathrm{T}} > 35$ GeV is required. In both regions, the b-tagged jet $|\eta|$ has to be lower than 2.5, and $|\eta|$ of the other jet(s) has to be smaller than 4.5. Additionally, exactly one forward (untagged) jet with $2.5 < |\eta| < 4.5$ is required, because the light quark is expected to have a large Lorentz boost along the beam axis. This allows the reduction of background events, as these are not expected to have forward jets.
For the leptons, the lepton with the largest p_{T} has to have $p_{\mathrm{T}} > 28$ GeV, the others $p_{\mathrm{T}} > 20$ GeV each. They are all required to have $|\eta| < 2.5$. The OSSF lepton pair has to have an invariant mass $|m_{\ell\ell} - m_Z| < 10$ GeV to limit background processes that did not produce a Z boson [27]. The cuts are summarised in Table 5.1.
The total MC yields of both signal regions with the background processes can be seen in Table 5.2. The background includes both processes with the same trileptonic final state as the tZq signal, and background with a "fake" lepton. This is emitted in a later process like another decay via a W boson, which produces additional leptons, and not in a primary interaction. Another source of fake leptons are jets wrongly reconstructed as leptons. Processes with similar final states (2/3 jets, 1 b jet, 3 leptons, 1 neutrino) can occur in multiple processes, the largest contributions coming from diboson and $t\bar{t}Z$ events.
In diboson events, if the Z and W bosons decay leptonically like required in the tZq final state, additional radiation jets can produce the same final state as in tZq. In $t\bar{t}Z$, the same trileptonic final state is reached if one of the b-jets from the top decays is not tagged correctly. For $t\bar{t}H$, $t\bar{t}W$ and tWZ the processes leading to the trileptonic final state are similar. In $t\bar{t}$ and Z + jets events it is not possible to directly reach the trileptonic final

Table 5.1.: Summary of the applied cuts.

Selection	Value
Lepton multiplicity	$= 3$
Lepton p_{T} [GeV]	>28 ; >20 ; >20
Lepton $\lvert\eta\rvert$	< 2.5
OSSF lepton pair multiplicity	$= 1$
OSSF lepton pair mass [GeV]	$\lvert m_Z - m_{\ell\ell}\rvert < 10$
Jet multiplicity	$= 2$ (SR1)
	$= 3$ (SR2)
Forward jet multiplicity	$= 1$
b jet multiplicity	$= 1$
b-tag WP	70 %
jet p_T [GeV]	> 35
untagged jet $\lvert\eta\rvert$	< 4.5
b jet $\lvert\eta\rvert$	< 2.5

state, therefore they contribute the fakes.
The $t\bar{t}$ + W or Z and tWZ samples are generated by MADGRAPH5_AMC@NLO [28] interfaced with PYTHIA 8 [29] using the A14 tune [30]. The $t\bar{t}$, $t\bar{t}H$ and tW samples are generated by POWHEGBOX [31] also interfaced with PYTHIA 8 using the A14 tune.
The Z + jets events are generated by SHERPA.2.2.1 [32].

Table 5.2.: Yields of the analysis. The uncertainties are all close to 0 and therefore not explicitly shown.

	SR1	SR2
tZq	41	65
$t\bar{t}H$	0	3
W/Z + Z/Z	14	59
$t\bar{t}W$	1	3
$t\bar{t}Z$	6	106
tWZ	2	24
Z + jets	3	4
$t\bar{t}$	5	10
Total	74	264

For this analysis, six observables are considered, which are all affected by the coupling between the top quark and Z boson. Since the Z boson originates from the top quark, their added momentum has to be conserved. Therefore, the coupling should also apply

to the transverse momentum. Additionally, the azimuth angle difference $\Delta\phi(t, Z)$ and the combined difference of ϕ and η with $\Delta R(t, Z) = \sqrt{(\Delta\phi)^2 + (\Delta\eta)^2}$ is also affected by the coupling between top and Z. Lastly, the masses of both Z boson and top quark are considered. The distributions of the observables are shown in Figure 5.1 for SR1 and in Figure 5.2 for SR2.

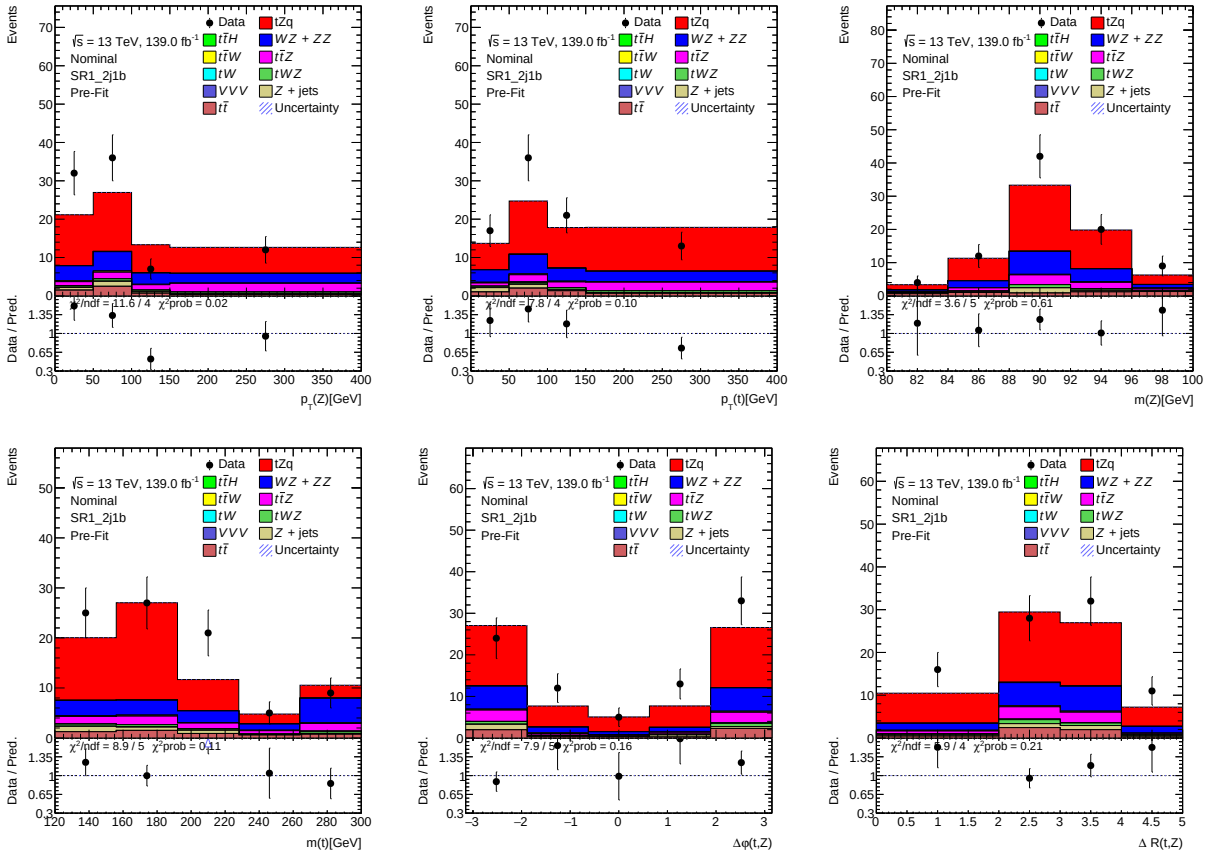

Figure 5.1.: Distributions of all observables in SR1.

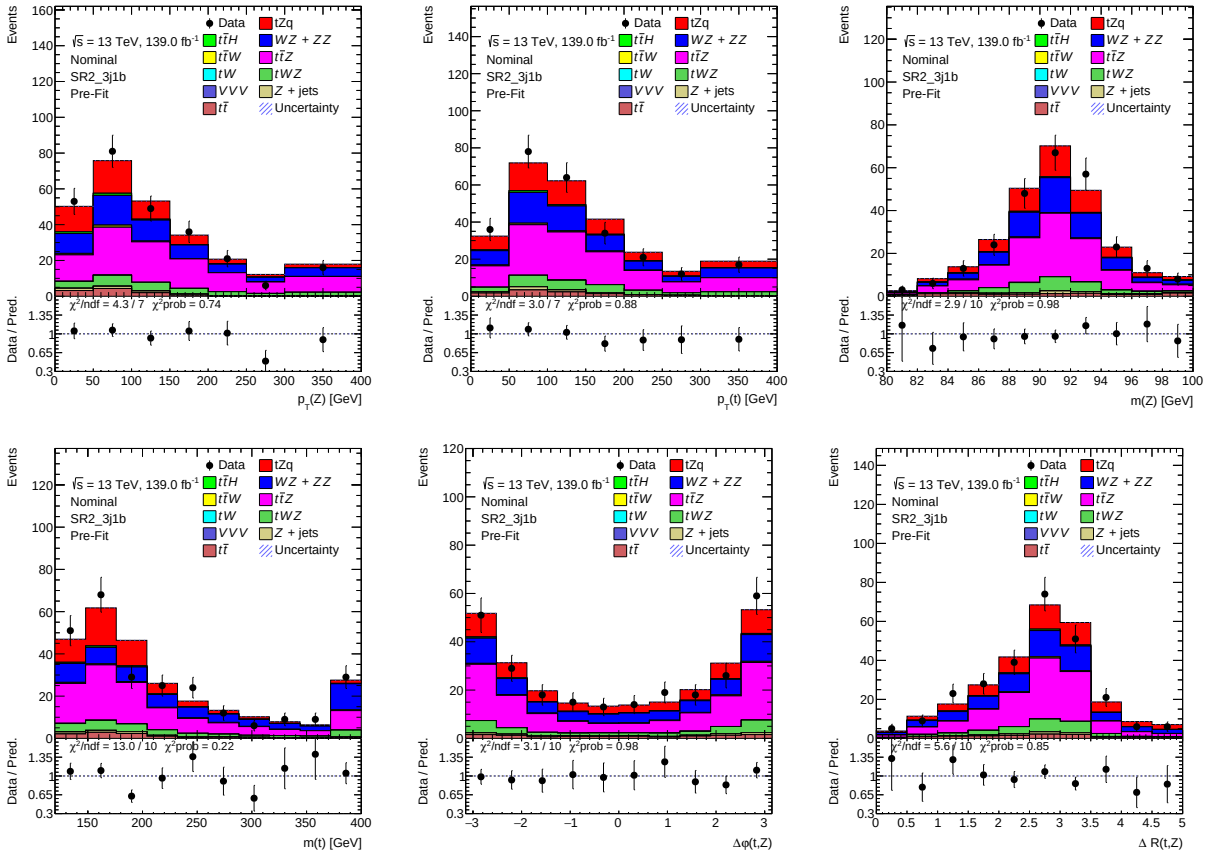

Figure 5.2.: Distributions of all observables in SR2.

5.3. Comparison between SM and SMEFT tZq samples

For the distributions in Figures 5.1 and 5.2, SM tZq files at next-to-leading order generated by MADGRAPH interfaced with PYTHIA 8 were used. To study the SMEFT operators, these are compared to SMEFT tZq files, which are generated at leading order by MADGRAPH, to evaluate the difference between them. In Figure 5.3, the transverse momentum of the Z boson is shown for both. In both SRs, the number of events is lower if only leading order processes are considered.

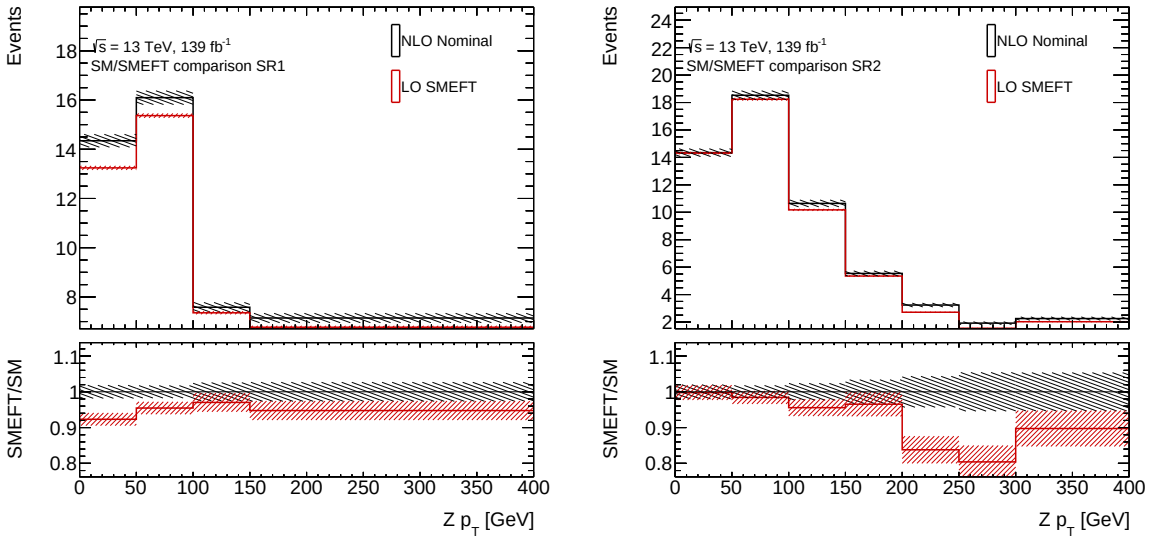

Figure 5.3.: Comparison for both tZq samples in both SRs in Z p_{T}.

6. Projected sensitivity of kinematic observables

The first goal in the EFT analysis is the identification of observables most sensitive to the operators. Therefore, the distributions of the observables $p_{\mathrm{T}}(Z)$, $p_{\mathrm{T}}(t)$, m(Z), m(t), $\Delta\phi(t, Z)$ and $\Delta R(t, Z)$ are studied.
The EFT operators $\mathcal{O}_{tW}$ and $\mathcal{O}_{tB}$ affect the cross section and shape of the distributions because of their influence on the top-Z coupling, which consequently can change the behaviour of the Z boson emission from the top. To find the observables most sensitive to the operators, the distributions of the obervables were visualised for the different Wilson coefficients and without their impact (nominal sample) as a reference. The impact of the EFT operators is primarily modelled by the assigned Wilson coefficient. Since the WCs are not identical for the different operators in the MC sample, 1 on 1 comparisons are not possible. The WCs for the imaginary part of $\mathcal{O}_{tB}$ are two times the ones for the real part, effectively doubling the impact compared to identical coefficients.
For all operators, the distributions of the p_{T} of both Z and top quark are the most sensitive observables. The $\mathcal{O}_{tW}$ p_{T} distributions are presented in Figure 6.1, with sensitivity being highest in the last bin in SR1 between 150 and 400 GeV with a 40% increase in the number of events in this bin compared to nominal. In SR2 a 200 % increase in the bin from 300 to 400 GeV is observed. In the appendix, the distributions for the masses of the top and Z are shown (Figure A.1), but their sensitivity is lower compared to the transverse momentum, while $\Delta\varphi(t, Z)$ and ΔR are shown in the appendix in Figure A.2, but display even less sensitivity than the masses.
For the $\mathcal{O}_{tB}$ operator, the p_{T} distributions for both real (Figure 6.2) and imaginary (Figure 6.3) part of the operator show a low sensitivity overall, with the real part of the operator showing only up to 5% difference. From this, it is possible to conclude that the $\mathcal{O}_{tB}$ operator is not suitable for analysis in the tZq process. The imaginary part is more sensitive, but still only reaches up to 5% in SR1 and 10 % difference in the sensitive bins. In the mass distributions (Figures A.3 and A.5) and the angular observables (Figures A.4 and A.6), the sensitivity is equally low.

Considering the difference in WCs, both parts of $\mathcal{O}_{tB}$ show similarly low effects on the distributions. The values of the WCs of $\mathcal{O}_{tW}$ are in between the $\mathcal{O}_{tB}$ ones, but their effect is considerably larger. In conclusion, the $\mathcal{O}_{tW}$ operator is the most promising for further study.

The p_{T} observables show the highest sensitivity and are therefore the focus in the analysis. The masses are considered as well, while the angular observables will not be considered furthermore.

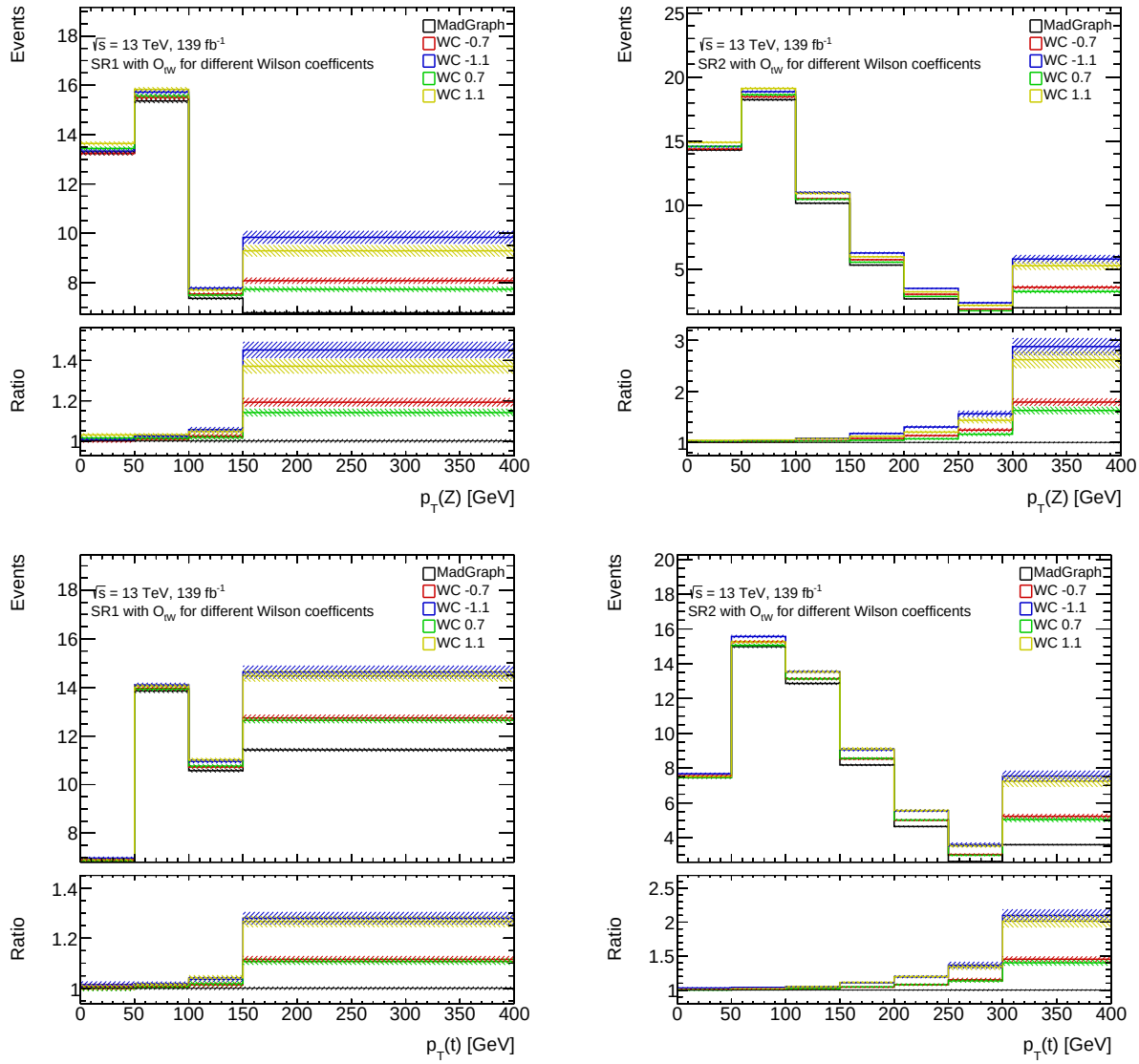

Figure 6.1.: Distributions of the p_{T} of the Z boson and top quark for both SRs with influence of the $\mathcal{O}_{tW}$ operator for different Wilson coefficients.

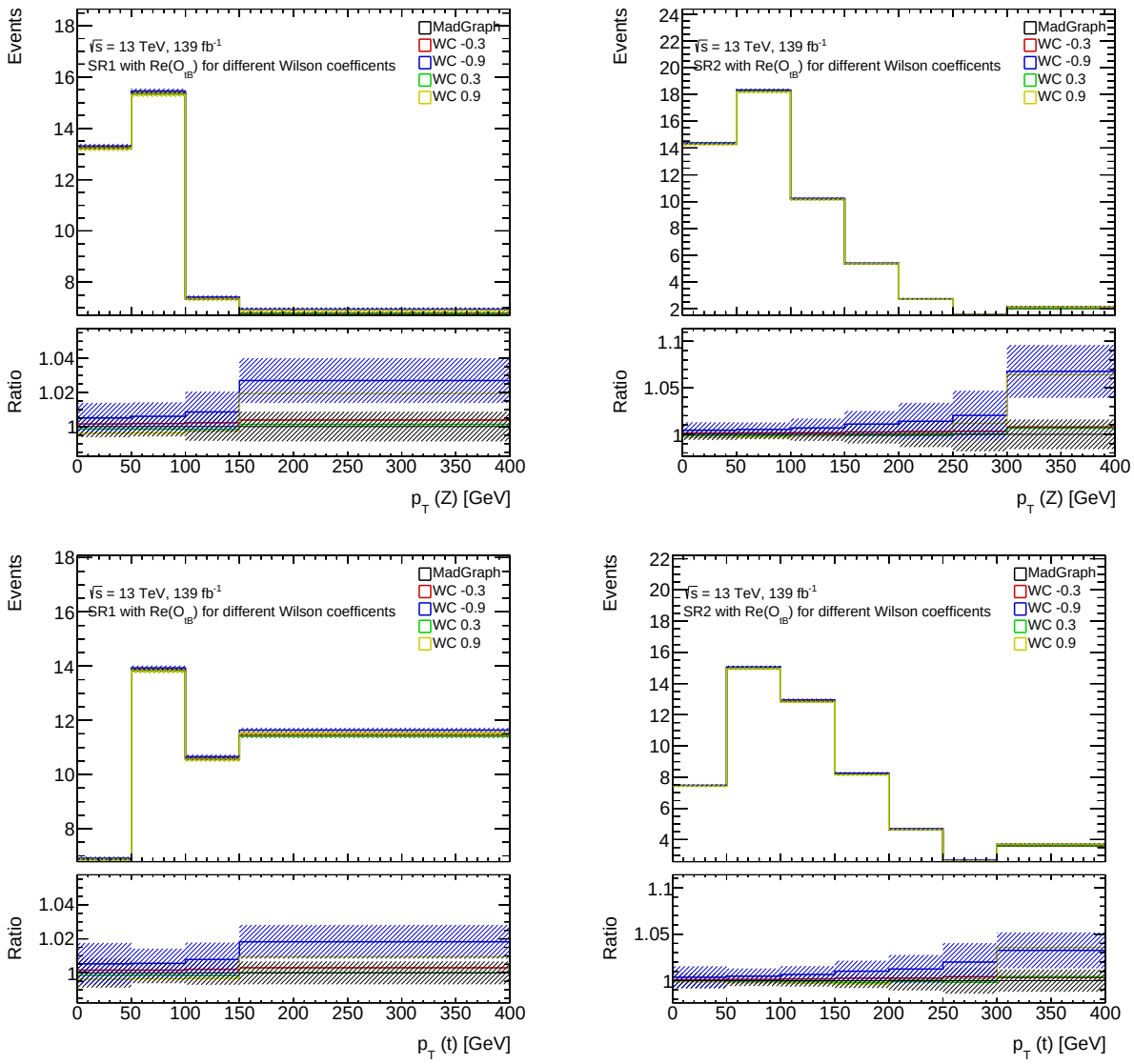

Figure 6.2.: Distributions of the p_{T} of the Z boson and top quark for both SRs with influence of the real part of the $\mathcal{O}_{tB}$ operator for different Wilson coefficients. In the ratio plot, uncertainties are only shown on the WC with the highest difference for clarity.

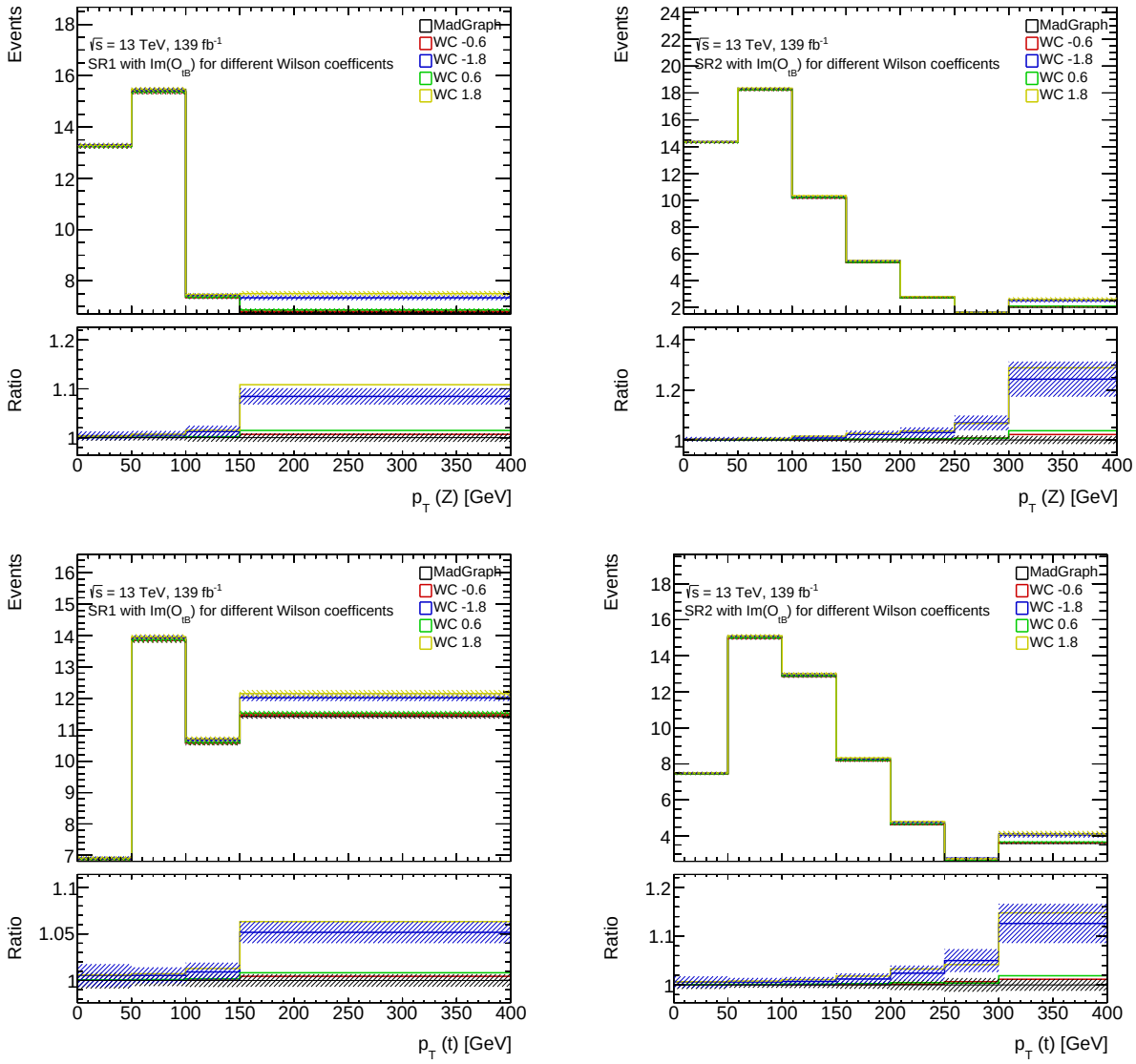

Figure 6.3.: Distributions of the p_{T} of the Z boson and top quark for both SRs with influence of the imaginary part of the $\mathcal{O}_{tB}$ operator for different Wilson coefficients. In the ratio plot, uncertainties are only shown on the WC with the highest difference for clarity.

Cross section differences

Table 6.1.: Cross section differences for the different operators.

Operator	WC	R SR1 [%]	R SR2 [%]
$\mathcal{O}_{tW}$	-0.7	5.38	6.25
	$+0.7$	4.41	5.33
	-1.1	12.85	15.03
	$+1.1$	11.33	13.59
$Re(\mathcal{O}_{tB})$	-0.3	0.19	0.19
	$+0.3$	-0.12	-0.09
	-0.9	0.84	0.91
	$+0.9$	-0.11	0.05
$\mathrm{Im}(\mathcal{O}_{tB})$	-0.6	0.14	0.16
	$+0.6$	0.22	0.30
	-1.8	1.52	1.88
	$+1.8$	1.77	2.29

To quantify the differences seen in the previous chapter, a metric is defined. It shows the difference between the SM cross section and the cross section with impact of the EFT operators, expressed as the ratio

$$R = \frac{N_{\mathrm{EFT}}}{N_{\mathrm{SM}}} - 1$$

where N is the number of events for EFT and SM respectively. This is calculated for all operators and their Wilson coefficients, the results are summarised in Table 6.1. The $\mathcal{O}_{tW}$ clearly has the largest difference in cross section even considering the different WCs. For the $\mathcal{O}_{tB}$ operator the cross section differences are similar for the negative coefficients taking the difference in the WC into account, but for the positive coefficients there are less events than in the nominal sample. For the imaginary part the behaviour is similar to $\mathcal{O}_{tW}$.
The differences between $\mathcal{O}_{tW}$ and $\mathcal{O}_{tB}$ could be explained by the additional influence in the bWt coupling, which can lead to a higher cross section of single top events.

Wilson coefficient fits

The observables which show the highest sensitivity are the transverse momentum of both Z boson and top quark. Therefore, the further analysis will focus on these. To quantify the qualitative results of the distributions, binned likelihood fits for the deviation in the

cross section in dependence of the WCs were produced. The fits consider statistical uncertainties only in this analysis, neglecting systematic uncertainties. The WCs are the parameter of interest of the fit, their impact on the bin contents is parameterised by a quadratic function.
In Figure 6.4, the fits for $\mathcal{O}_{tW}$ are presented, clearly showing a quadratic, but not symmetrical, behaviour and reaching up to an 50 % increase in cross section in the last bin for SR1, and 200 % in SR2. The fits explicitly show that the influence is highest in the last bins with high p_{T} and are consistent with the sensitivity study.
Since the fits use the WCs as the variable, the fits give continuous distributions, therefore it is possible to directly compare the impact of the operators at the same WC. For the $\mathcal{O}_{tB}$ operator, the fits display similar behaviour, but to a lower level. The real part (Figure 6.5) reaches a 10% increase in cross section, which is low compared to the $\mathcal{O}_{tW}$ operator. The imaginary part (Figure 6.6) shows better sensitivity than the real one, but only reaches 15 % increase in SR1, and 40 % increase in SR2, only a fifth of the $\mathcal{O}_{tW}$ operator.
As a first conclusion based on the sensitivity, the p_{T} observables are expected to produce the best limits on the WCs, because they show the highest sensitivity.

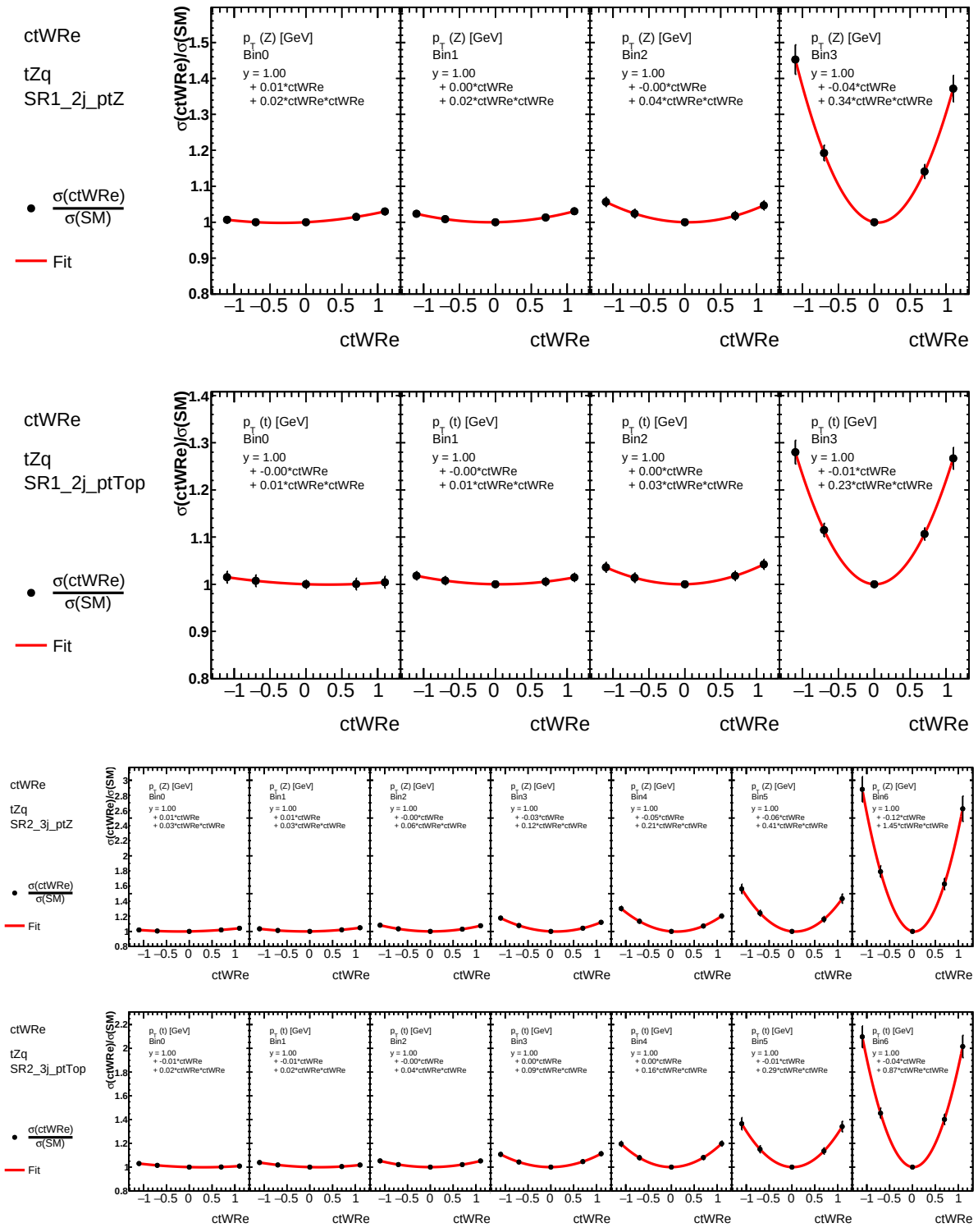

Figure 6.4.: Fits for the p_{T} in both SRs for the $\mathcal{O}_{tW}$ operator.

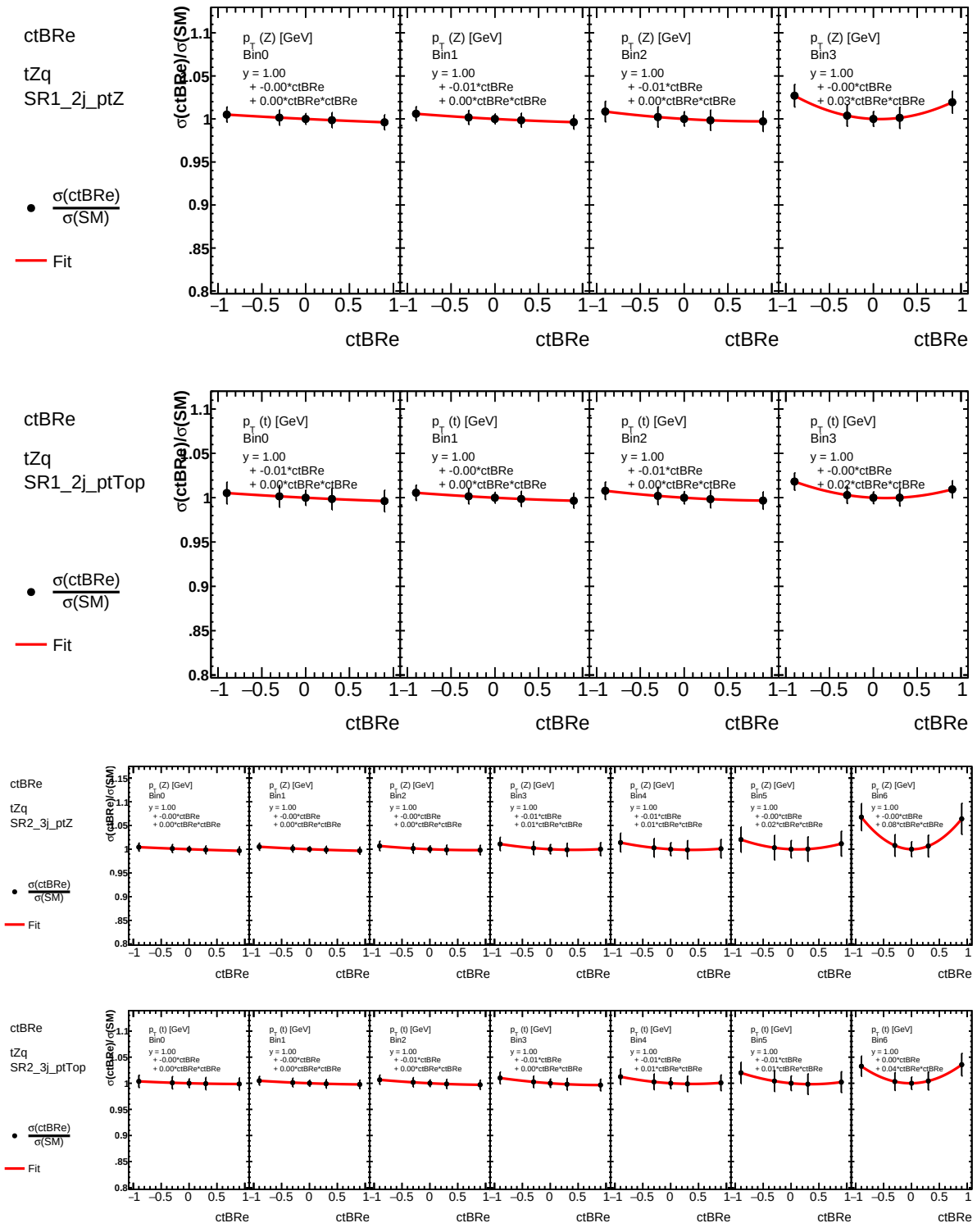

Figure 6.5.: Fits for the p_{T} in both SRs for the real part of the $\mathcal{O}_{tB}$ operator.

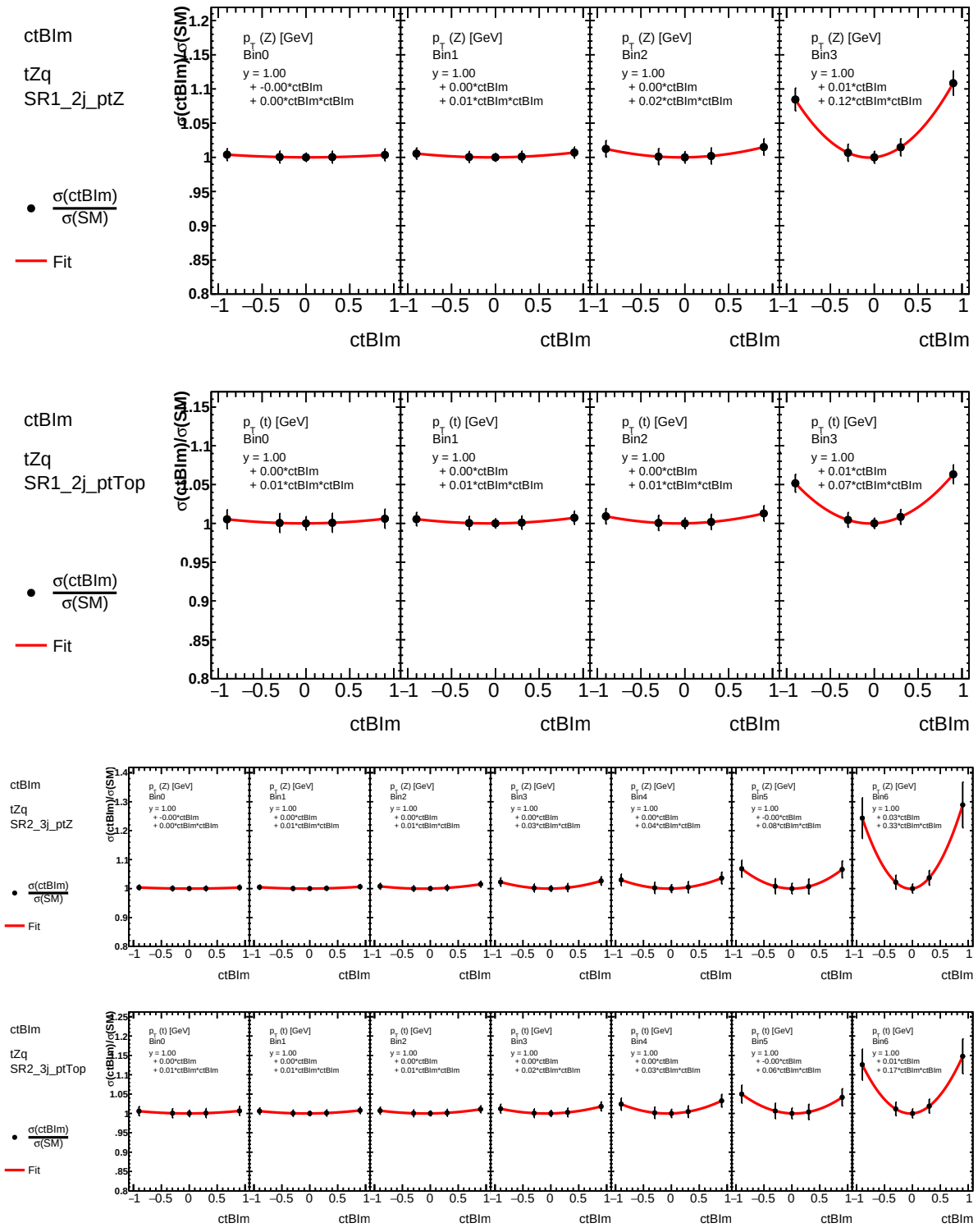

Figure 6.6.: Fits for the p_{T} in both SRs for the imaginary part of the $\mathcal{O}_{tB}$ operator.

7. Results

Table 7.1.: Summary of all calculated exclusion limits.

Operator	Observable	Exclusion Limits ($1\sigma/2\sigma$)
O_{tW}	Z p_T	[-0.98;1.07] / [-1.44;1.53]
	Z mass	[-1.35;1.39] / [-1.93;1.97]
	top p_T	[-0.99;1.02] / [-1.46;1.49]
	top mass	[-1.32;1.35] / [-1.88;1.92]
$Re(O_{tB})$	Z p_T	[-3.78;3.96] / [-5.59;5.78]
	Z mass	[-4.83;5.50] / [-7.16;7.82]
	top p_T	[-4.00;4.28] / [-5.88;6.16]
	top mass	[-4.80;5.65] / [-7.13;7.96]
$Im(O_{tB})$	Z p_T	[-1.95;1.86] / [-2.84;2.75]
	Z mass	[-2.54;2.43] / [-3.66;3.56]
	top p_T	[-2.08;2.00] / [-3.00;2.92]
	top mass	[-2.53;2.43] / [-3.65;3.55]

For the final results the likelihood functions are fitted, and their negative logarithm is minimised. Based on this, the 68 % (1σ) and 95 % (2σ) confidence intervals are calculated. The results are summarised in Table 7.1. The calculation shows that both p_{T} observables are best suitable for this analysis, which was already expected from the sensitivity study based on the distributions. Their likelihood distributions can be seen in Figure 7.1. Once again the different sensitivity can be estimated from the value of the log-likelihood function. The log-likelihood curve of the $\mathcal{O}_{tW}$ operator is rising the fastest outside the exclusion limits, already being at a value of 23 for Wilson coefficients of 3, while the imaginary part of $\mathcal{O}_{tB}$ only reaches a value of 14. The real part reaches a value of 14 for a WC of 10, the scale from -3 to 3 is not sufficient to determine both confidence intervals, once again showing the sensitivity is low.

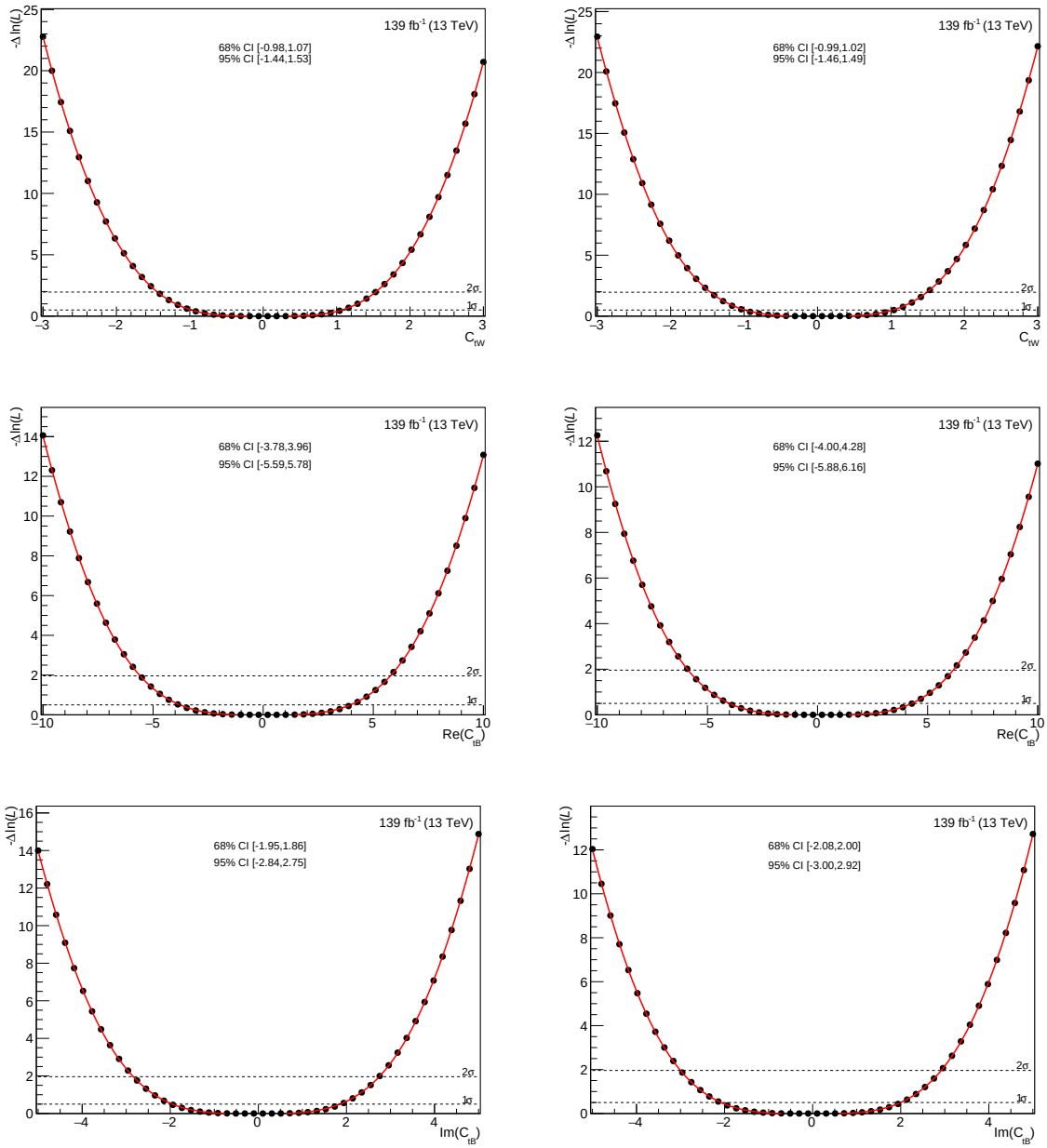

Figure 7.1.: Likelihood distributions of the operators for Z p_{T} (left) and top p_{T} (right) with the confidence levels shown as dotted lines, and the calculated confidence intervals.

8. Conclusion

Table 8.1.: Best exclusion limits on the 95 % confidence level for the three operators.

Observable	Operator	Excl. Limit
Z p_{T}	O_{tW}	[-1.44;1.53]
	$\mathrm{Re}(\mathrm{O}_{tB})$	[-5.59;5.78]
	$\mathrm{Im}(\mathrm{O}_{tB})$	[-2.84;2.75]
top p_{T}	O_{tW}	[-1.46;1.49]
	$\mathrm{Re}(\mathrm{O}_{tB})$	[-5.88;6.16]
	$\mathrm{Im}(\mathrm{O}_{tB})$	[-3.00;2.92]

After analysing the deviations in the distributions of the observables, quantifying these and fitting the impact of the Wilson coefficients, the exclusion limits are calculated. These show that the p_{T} observables are most useful to study the limits of the impact of the $\mathcal{O}_{tW}$ and $\mathcal{O}_{tB}$ operator.

In this analysis, the tZq process is most sensitive to the $\mathcal{O}_{tW}$ operator, while having low sensitivity to the $\mathcal{O}_{tB}$ operator, especially the real part of it. This was already expected from the definitions of the operators, as the $\mathcal{O}_{tW}$ operator influences multiple couplings. The exclusion limits for the best results of the 95 % confidence level are summarised in Table 8.1.

For future EFT studies in the tZq process, the $\mathcal{O}_{tW}$ operator is the logical choice, while for the $\mathcal{O}_{tB}$ operator the imaginary part is a better choice than the real part. To increase the quality of the results, this analysis should be repeated with the inclusion of systematic uncertainties, since they were not considered in this analysis, but will definitely impact the value of the exclusion limits.

A. Appendix

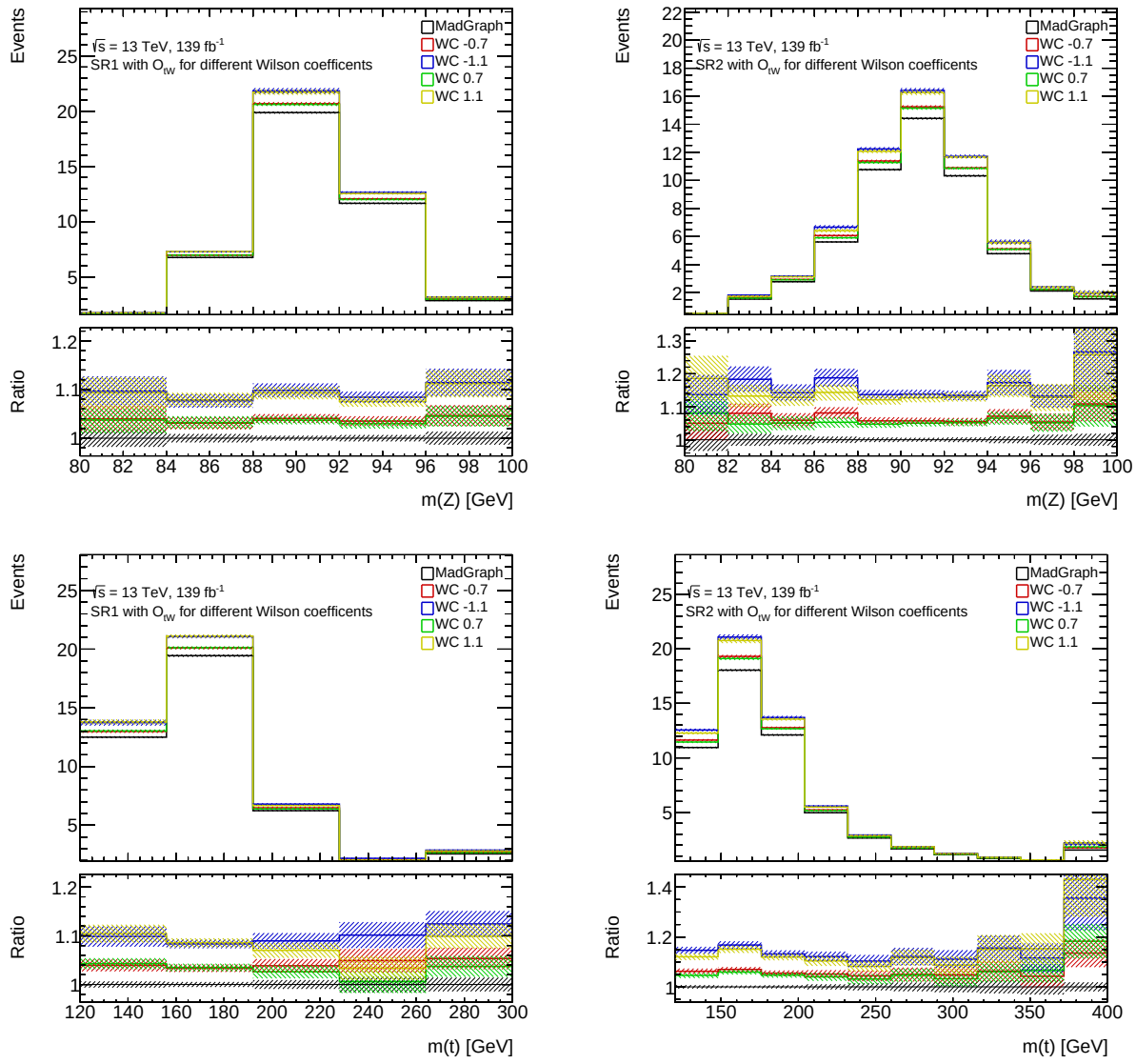

Figure A.1.: Distributions of the mass of the Z boson and top quark for both SRs with influence of the $\mathcal{O}_{tW}$ operator for different Wilson coefficients.

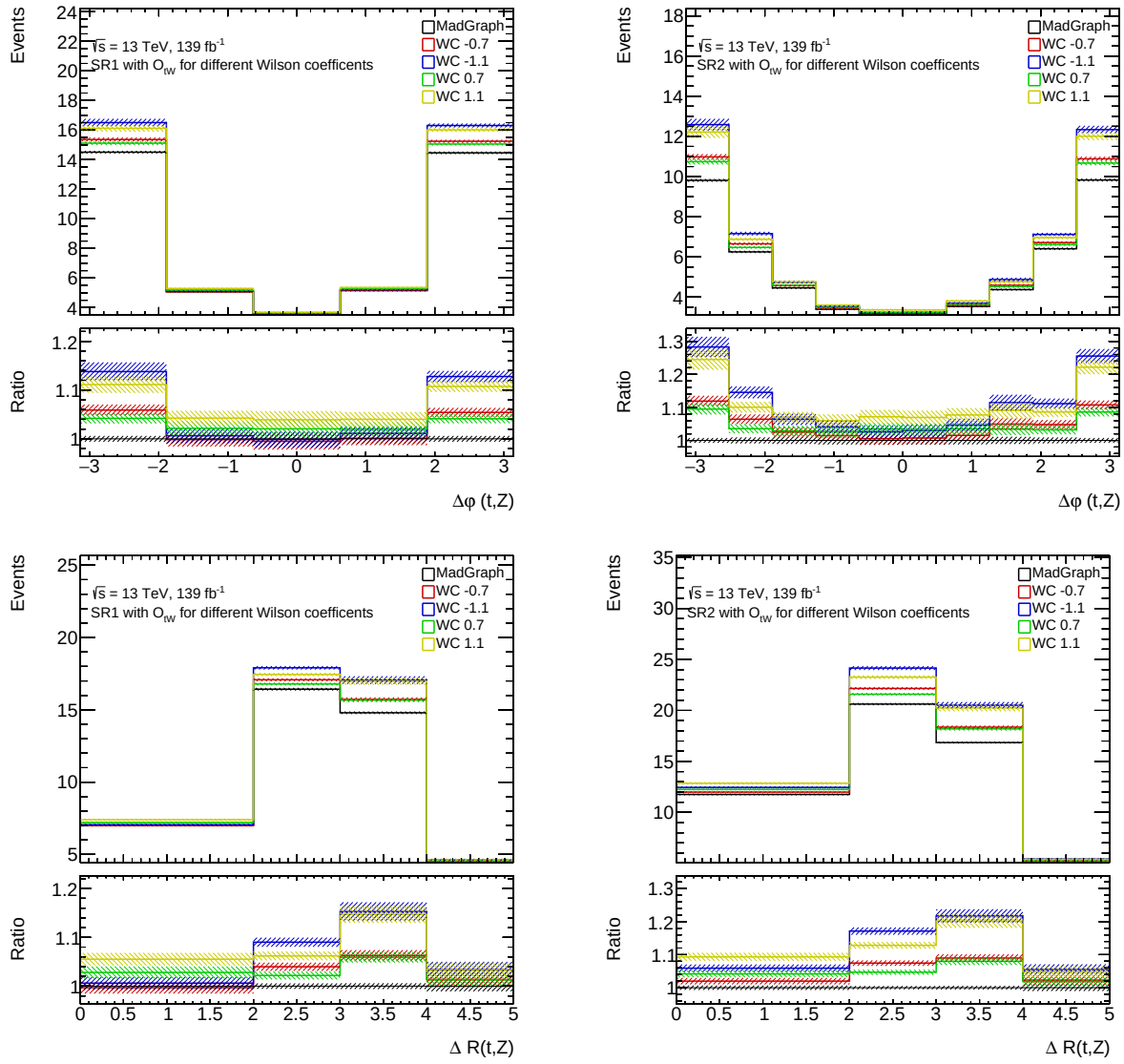

Figure A.2.: Distributions of the angular observables between the Z boson and top quark for both SRs with influence of the $\mathcal{O}_{tW}$ operator for different Wilson coefficients.

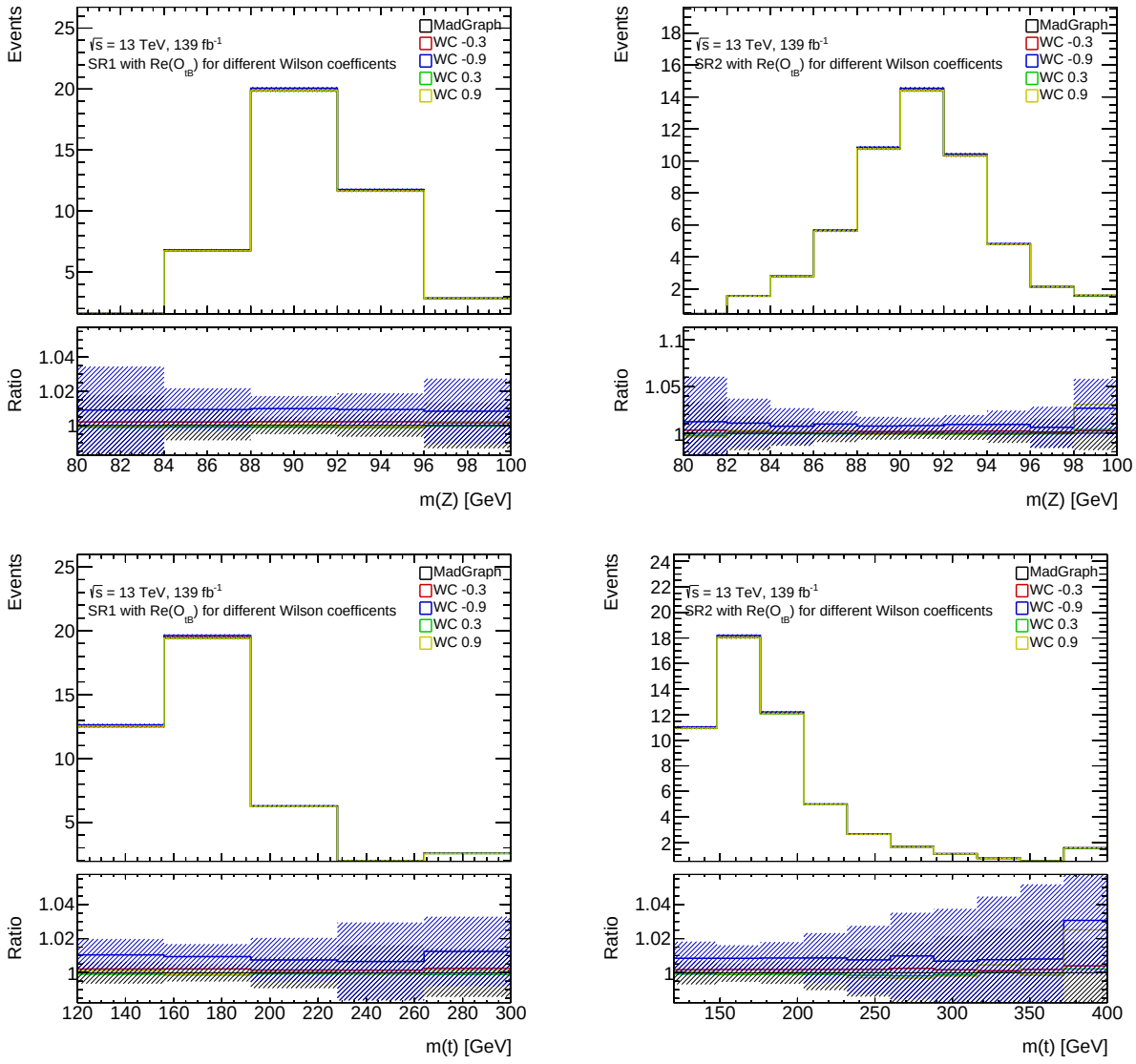

Figure A.3.: Distributions of the mass of the Z boson and top quark for both SRs with influence of the $\mathcal{O}_{tB}$ operator for different Wilson coefficients. In the ratio plot, uncertainties are only shown on the WC with the highest difference for clarity.

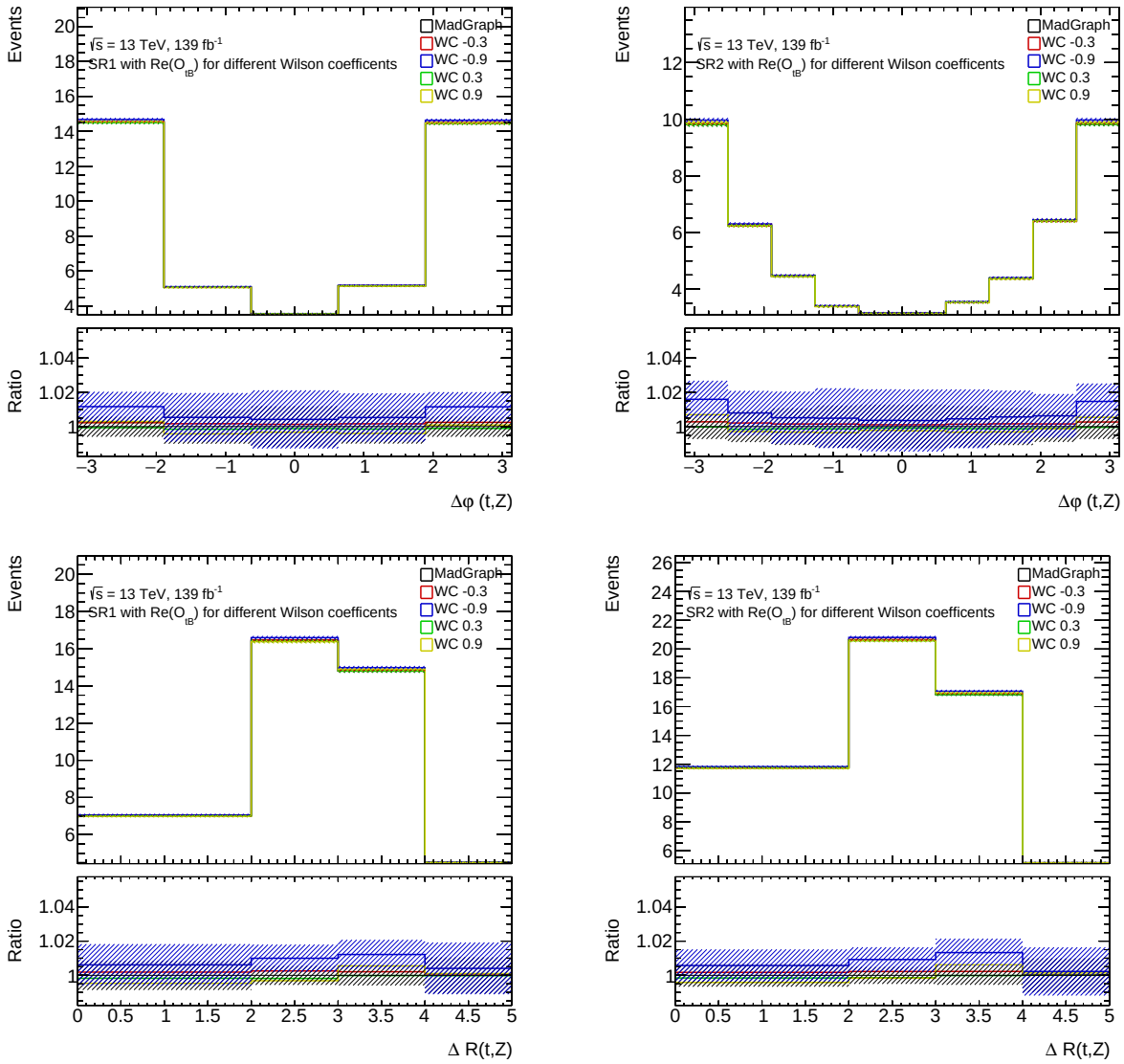

Figure A.4.: Distributions of angular observables between the Z boson and top quark for both SRs with influence of the $\mathcal{O}_{tB}$ operator for different Wilson coefficients. In the ratio plot, uncertainties are only shown on the WC with the highest difference for clarity.

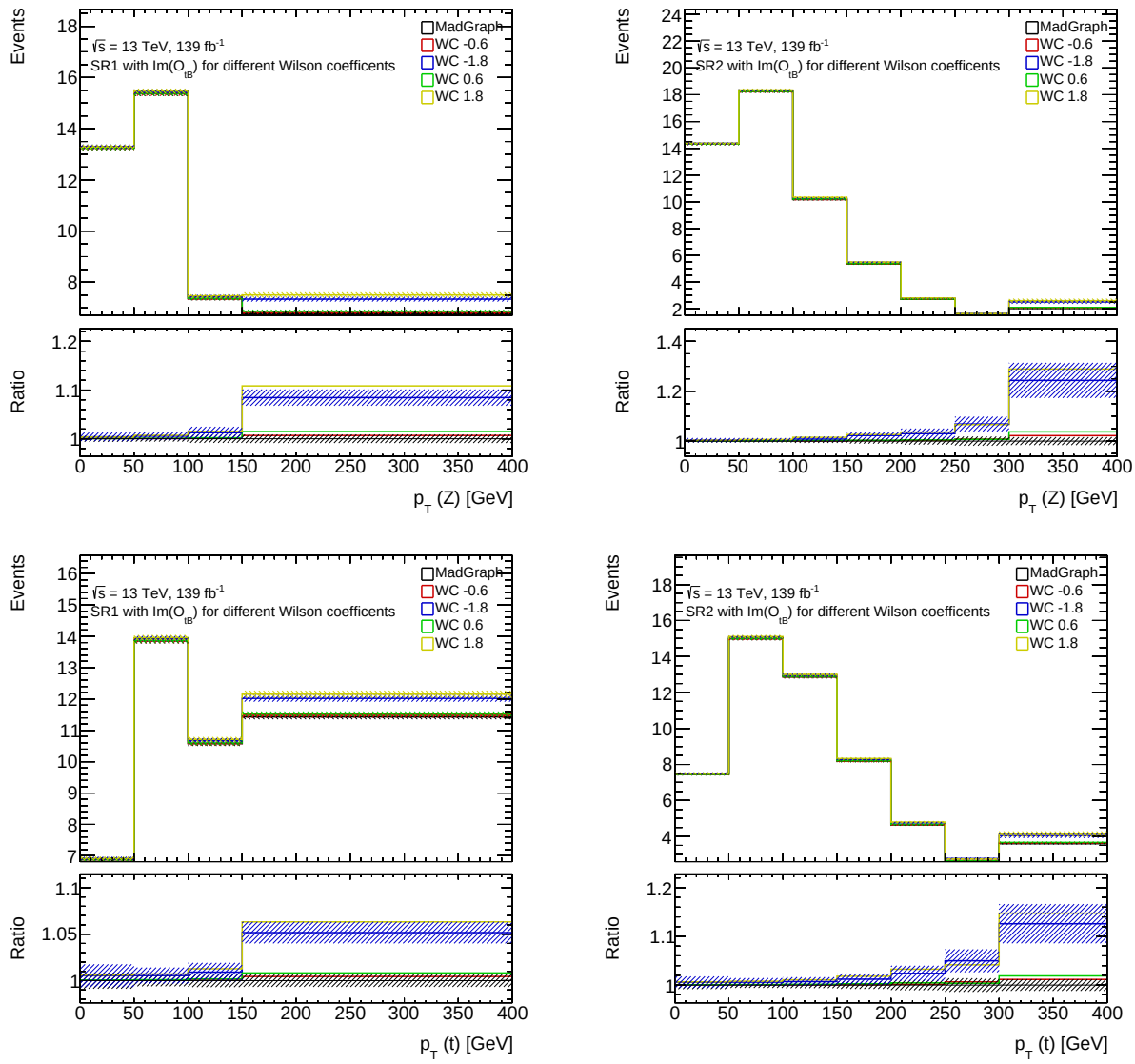

Figure A.5.: Distributions of the mass of the Z boson and top quark for both SRs with influence of the $\mathcal{O}_{tW}$ operator for different Wilson coefficients.In the ratio plot, uncertainties are only shown on the WC with the highest difference for clarity.

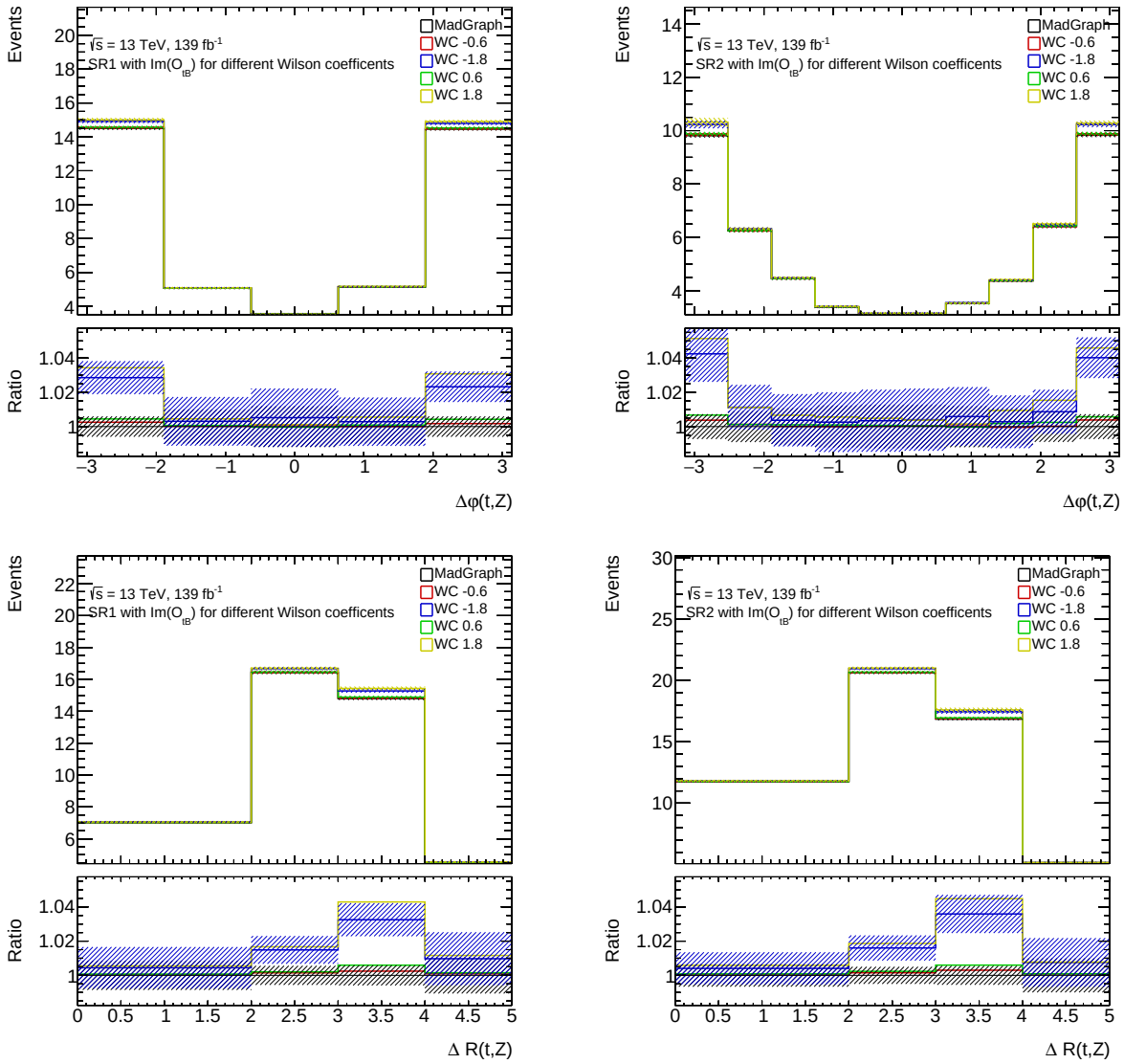

Figure A.6.: Distributions of the angular observables between the Z boson and top quark for both SRs with influence of the $\mathcal{O}_{tW}$ operator for different Wilson coefficients.In the ratio plot, uncertainties are only shown on the WC with the highest difference for clarity.

Bibliography

[1] W. J. Marciano, H. Pagels, *Quantum Chromodynamics: A Review*, Phys. Rept. **36**, 137 (1978)

[2] A. Salam, *Weak and Electromagnetic Interactions*, Conf. Proc. C **680519**, 367 (1968)

[3] Bigi et al., *Production and decay properties of ultra-heavy quarks*, Phys. Lett. B **181**, 157 (1986)

[4] ATLAS Collaboration, *Measurement of the W-boson mass in pp collisions at* $\sqrt{s}$ = 7 TeV *with the ATLAS detector*, Eur. Phys. J. C **78(2)** (2018)

[5] Arnaudon et al., *Measurement of the mass of the Z boson and the energy calibration of LEP*, Phys. Lett. B **307** (1993)

[6] P. W. Higgs, *Broken Symmetries and the Masses of Gauge Bosons*, Phys. Rev. Lett. **13**, 508 (1964)

[7] ATLAS Collaboration, *Measurement of the Higgs boson mass in the* $H\rightarrow ZZ\rightarrow$ 4 ℓ *and* $H\rightarrow \gamma\gamma$ *channels with* $\sqrt{s}$ = 13 TeV *pp collisions using the ATLAS detector*, Phys. Lett. B **784**, 345 (2018)

[8] A. Castro (ATLAS, CMS), *Top Quark Mass Measurements in ATLAS and CMS*, in *12th International Workshop on Top Quark Physics* (2019), `hep-ex/1911.09437`

[9] S. Abachi, et al. (DØ Collaboration), *Observation of the Top Quark*, Phys. Rev. Lett. **74(14)**, 2632 (1995)

[10] F. Abe, et al. (CDF Collaboration), *Observation of top quark production in* $\bar{p}p$ *collisions*, Phys. Rev. Lett. **74**, 2626 (1995)

[11] CMS Collaboration, *Measurement of the associated production of a single top quark and a Z boson in pp collisions at* $\sqrt{s}$*=13* TeV, Phys. Lett. B **779**, 358 (2018)

[12] Super-Kamiokande Collaboration, *Evidence for Oscillation of Atmospheric Neutrinos*, Phys. Rev. Lett. **81(8)**, 1562 (1998)

[13] N. Aghanim, et al. (Planck), *Planck 2018 results. VI. Cosmological parameters*, Astron. Astrophys. **641**, A6 (2020)

[14] A. D. Sakharov, *Violation of CP invariance, C asymmetry, and baryon asymmetry of the universe*, JETP Lett. **5**, 24 (1967)

[15] C. Burgess, *An Introduction to Effective Field Theory*, Annu. Rev. Nucl. Part. Sci. **57(1)**, 329 (2007)

[16] A. Helset, A. Kobach, *Baryon number, lepton number, and operator dimension in the SMEFT with flavor symmetries*, Phys. Lett. B **800**, 135132 (2020)

[17] F. Maltoni, L. Mantani, K. Mimasu, *Top-quark electroweak interactions at high energy*, JHEP **10**, 004 (2019)

[18] ATLAS Collaboration, *The ATLAS Experiment at the CERN Large Hadron Collider*, JINST **3**, S08003 (2008)

[19] L. Evans, P. Bryant, *LHC Machine*, JINST **3(08)**, S08001 (2008)

[20] ALICE Collaboration, *The ALICE experiment at the CERN LHC*, JINST **3**, S08002 (2008)

[21] CMS Collaboration, *The CMS Experiment at the CERN LHC*, JINST **3**, S08004 (2008)

[22] LHCb Collaboration, *The LHCb Detector at the LHC*, JINST **3**, S08005 (2008)

[23] ATLAS Collaboration , *Electron and photon performance measurements with the ATLAS detector using the 2015–2017 LHC proton-proton collision data*, JINST **14(12)**, P12006 (2019)

[24] ATLAS Collaboration , *Muon reconstruction and identification efficiency in ATLAS using the full Run 2 pp collision data set at* $\sqrt{s} = 13$ TeV, Eur. Phys. J. C **81(7)**, 578 (2021)

[25] M. Cacciari, G. P. Salam, G. Soyez, *The anti-k_t jet clustering algorithm*, JHEP **04**, 063 (2008)

[26] ATLAS Collaboration , *ATLAS b-jet identification performance and efficiency measurement with* $t\bar{t}$ *events in pp collisions at* $\sqrt{s} = 13$ TeV, Eur. Phys. J. C **79(11)**, 970 (2019)

[27] ATLAS Collaboration, *Observation of the associated production of a top quark and a Z boson in pp collisions at* $\sqrt{s} = 13$ TeV *with the ATLAS detector*, JHEP **07**, 124 (2020)

[28] J. Alwall, et al., *The automated computation of tree-level and next-to-leading order differential cross sections, and their matching to parton shower simulations*, JHEP **2014(7)** (2014)

[29] T. Sjöstrand, et al., *An introduction to PYTHIA 8.2*, Comput. Phys. Commun. **191**, 159 (2015)

[30] ATLAS Collaboration , *ATLAS Pythia 8 tunes to 7* TeV *data* (2014)

[31] S. Frixione, G. Ridolfi, P. Nason, *A positive-weight next-to-leading-order Monte Carlo for heavy flavour hadroproduction*, JHEP **2007(09)**, 126 (2007)

[32] T. Gleisberg, et al., *Event generation with SHERPA 1.1*, JHEP **2009(02)**, 007 (2009)

Acknowledgement

First and foremost I want to thank Sreelakshmi and Steffen for all of the help over the 14 weeks. Without you this would not have been possible for me. Then I would like to thank to Professor Quadt, for giving me the opportunity to write my thesis in his working group, which I want to thank for the warm welcome and their comments regarding my work. Also a thank you to Professor Lai for agreeing to referee my thesis. I would also like to thank Josh McFayden for the help with EFTRexFitter.
Furthermore, I have to thank my family and friends, as without your support this would not have been possible.

Erklärung nach §13(9) der Prüfungsordnung für den Bachelor-Studiengang Physik und den Master-Studiengang Physik an der Universität Göttingen:
Hiermit erkläre ich, dass ich diese Abschlussarbeit selbständig verfasst habe, keine anderen als die angegebenen Quellen und Hilfsmittel benutzt habe und alle Stellen, die wörtlich oder sinngemäß aus veröffentlichten Schriften entnommen wurden, als solche kenntlich gemacht habe.
Darüberhinaus erkläre ich, dass diese Abschlussarbeit nicht, auch nicht auszugsweise, im Rahmen einer nichtbestandenen Prüfung an dieser oder einer anderen Hochschule eingereicht wurde.

Göttingen, den 16. Januar 2023

(Tim Schlömer)